Remote Sensing Image Compression in Visible/Near-Infrared Range Using Heterogeneous Compressive Sensing

Jin Li, Yao Fu, Guoning Li, and Zilong Liu

***Abstract*—Compressive sensing (CS) framework is very suitable for onboard image compression of high-resolution remote sensing cameras in the visible/near-infrared range (VI/NI-RSC) because it has the low-complexity in the sampling measurement stage. In this paper, we propose a new heterogeneous CS method for VI/NI-RSCs. Different from conventional CS methods evenly allocating sensing resources, the proposed method fully employs texture-feature information of remote sensing images to guide the allocation of sensing resources. More sensing resources are allocated to high-frequency regions, but fewer to low-frequency regions. The heterogeneous distribution of sensing resources obtains high reconstruction quality at the same compression performance, as well as high compression performance at the same level reconstructed quality. The shift of sensing resources is consistent with artificial image interpretations, i.e., human visual characteristics, where high-frequency regions, such as edges and textures, are the principal proof of the ground target identification. Experimental results indicate that the proposed method has better reconstruction quality than conventional CS method where texture-features are not utilized.**

***Index Terms*—Heterogeneous compressive sensing (CS), panchromatic images, remote sensing image compression.**

I. Introduction

HIGH-RESOLUTION remote sensing panchromatic cameras (RSPC), i.e., visible/near-infrared bands, are essential tools in earth observation applications [1]–[5]. In an RSPC, the acquiring and processing of sensing panchromatic images (RSPI) approximately conform to the Nyquist sampling theory (NST) under the condition of noiseless. The sampling rate of an image sensor of RSPCs is at least twice the maximum frequency of a two-dimensional (2-D) scene. Inside an RSPC, a video processor, extracting photo-induced charges and converting analog images into digital images, is also performed at the NST framework.

Under the NST-based imaging frameworks, the captured images have the large redundancies of neighboring pixels. However, current on-orbit memories and downlink width of a spacecraft are limited [6], [7]. Therefore, it is necessary to establish a high-performance compression of remote sensing images [8]–[11] for RSPCs.

Different from conventional NST-based sampling methods, compressive sampling (CS) is a novel unconventional method in image acquisition and compression. In the CS theory framework, 2-D images can be reconstructed from significantly fewer samples or measurements [12], [13]. Under the CS-based imaging framework, the redundancies of neighboring pixels captured images do not exist. Under current limited downlink transmission bandwidth and limited on-orbit storage resources, the CS-based compression framework is very suitable for RSPCs. Recently, many CS schemes in the compression of remote sensing optical cameras have been proposed [14]–[17]. Fully different from the ground part, an RSPC compression algorithm requires a low-complexity encoder because it is usually completed on board, where the energy and memory resources are limited. Moreover, an on-orbit compressor of an RSPC usually has the requirements of convenient implementation on a hardware platform, such field-programmable gate array (FPGA) processors. CS is very suitable for the compressor of the RSPC. Currently, CS has been used in the encoder of images or videos [18]–[20]. Different CS compression methods are proposed for different applied cases [21], [22]. In [22], Deng *et al*. used CS in combination with statistical properties of DWT coefficients to implement an image coding. They used different CS resources for low-band and high-bands. However, they do not consider internal content characteristics of a high subband. In addition, CS can also be applied to multicomponent (multispectral or hyperspectral) images, such as compressive hyperspectral imaging (CHI) [23] and unmixing of hyperspectral data [18]. Currently, the CS theory focused on the CHI, such as blind compressive sensing [24], spatial-spectral encoded CIH [25]. In [26], Yang *et al*. demonstrated a compressive hyperspectral imaging method which recovered a large range of scenes with a small number of sensors via CS theory. Current works have not yet applied CS scheme to multispectral and hyperspectral image compressions based on internal content characteristics of a spectral-band.

Currently, the wavelet-based CS focuses on the even allocation of sensing resources in a wavelet-band. When remote sensing images with abundant texture and edge features perform the sparse transform using a DWT basis, a large number of large-amplitude high-frequency coefficients are produced,

Manuscript received April 24, 2018; revised July 26, 2018 and September 3, 2018; accepted October 17, 2018. Date of publication December 25, 2018; date of current version December 31, 2018. This work was supported in part by the Natural Science Foundation of China under Grant 61505093 and Grant 61505190, and in part by the National Key Research and Development Plan of China under Grant 2016YFC0103600. *(Corresponding authors: Guoning Li and Zilong Liu.)*

J. Li is with the Photonics and Sensors Group, Department of Engineering, University of Cambridge, Cambridge CB3 0FA, U.K. (e-mail: jl918@cam.ac.uk).

Y. Fu and G. Li are with the Changchun Institute of Optics, Fine Mechanics and Physics, Chinese Academy of Sciences, Changchun 130033, China (e-mail: fuyao@ciomp.ac.cn; lgn_ciomp@163.com).

Z. Liu is with Optic Division, National Institute of Metrology, Beijing 100029, China (e-mail: liuzl@nim.ac.cn).

Color versions of one or more of the figures in this paper are available online at http://ieeexplore.ieee.org.

Digital Object Identifier 10.1109/JSTARS.2018.2879363

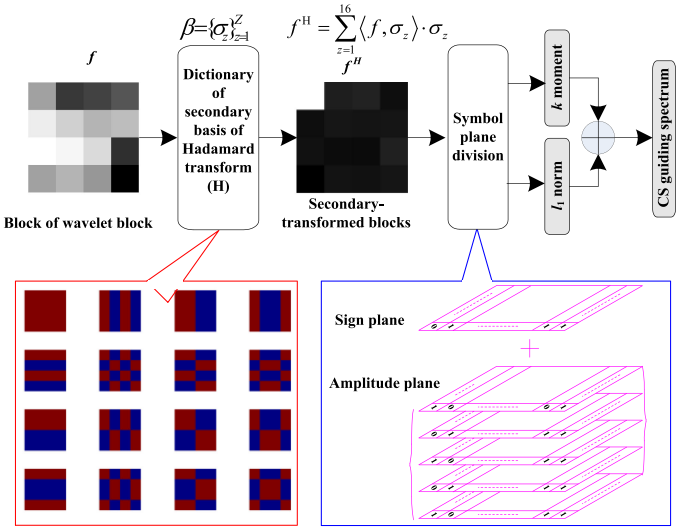

Fig. 1. Extraction algorithm of CS guiding map.

while the low-frequency area has small amplitude coefficients even zero regions. In the even allocation method, sensing resources are wasted to the low-frequency areas, but not enough to high-frequency areas. Here, we propose a heterogeneous compressive sensing (HCS), which fully employs wavelet feature information of images and allocate more sensing resources to high-amplitude regions, but fewer to low-amplitude regions in the same wavelet subband. Because high-amplitude regions represent high-frequency information of images, the more sensing resources would obtain the better quality of the edge and texture features of images. This new idea is consistent with the recognizing of remote sensing images using artificial image interpretations. In addition, HSC in principle can also be used for multispectral and hyperspectral images via three feasible schemes. The first scheme is that a spectral decorrelation transform (e.g., KLT) is first used to remove spectral redundancies, and then HCS is applied to each band to remove spatial redundancies. In the second scheme, HCS may be applied to spectral dimension after or before a spatial transform (e.g., DWT). Finally, the HCS may be applied to both spatial and spectral dimension.

II. Proposed Algorithm

We use a secondary transform to guide the allocation of sensing resources. The secondary transform has two functions: the establishing of CS guiding spectrum (CS-GS) and the performing of secondary-transform CS. The first function can implement the CS-GS to guide the allocation of sensing resources to high-frequency and low-frequency areas. The second function can implement the CS in the secondary domain to compensate for the drawback of DWT in the sparse representation of remote sensing images. We first use our CS guiding spectrum detection (CS-GSD) algorithm to obtain the CS-GS, indicating spatial frequency information in a panchromatic image. Fig. 1 shows the principle of the CS-GSD algorithm. First, an image performs the wavelet transform to obtain the wavelet blocks. Then, wavelet coefficients are organized into several nonoverlapped wavelet blocks (NOWB). The size of each NOWB is 4×4 pixels. We use f to express an NOWB. In an NOWB, we use Z to denote the number of wavelet coefficients, i.e., $Z = 16$.

We consider an NOWB as a vector, which is composed of Z elements in R^Z. We use β to express a secondary orthonormal transform basis, which is composed of M vectors of R^M. We use σ_z,$z \in [1, Z]$, to denote a base vector of β. The secondary orthonormal transform vector is expressed by $\beta = \{\sigma_z\}_{z=1}^{Z}$.

We use f^H to express to a representation of the vector f on the secondary transform basis β, which can be expressed as follows:

$$f^H = \sum_{z=1}^{Z} \langle f, \sigma_z \rangle \cdot \sigma_z = \sum_{z=1}^{Z} c[z]\sigma_z \tag{1}$$

where $c[z]$ is the secondary transform coefficients. We use the secondary transform coefficients to implement the aforementioned two functions, i.e., extracting the CS-GS and the sensing measurement. We use a Hadamard transform (HT) as the secondary orthogonal transform because it has very low complexity and convenient hardware implementation. In the case of enough onboard computation resources, other high-performance transform bases, such as DCT, PCA, beyond wavelets, etc., are also available as the secondary transform. We define two planes: a sign plane and an amplitude plane. The sign plane is composed of all signs of the secondary transformed coefficients in an NOWB. The amplitude plane is composed of all amplitude of the secondary transformed coefficients in an NOWB. Let F be the transform coefficient of an image block f. First, we use a sign function to extract the sign of F as follows:

$$F_s = \text{sign}(F). \tag{2}$$

We calculate the inverse transform of F_s as follows:

$$f_s = C^t \bullet F_s \bullet C. \tag{3}$$

The CS-GSD of the sign part can be calculated as follows:

$$f_{sa} = \text{abs}(f_s) \tag{4}$$

$$\text{GSD}_1 = G * {f_{sa}}^2 \tag{5}$$

where sign $(\cdot)$ is a sign function and G is a 2-D Gaussian low-pass filter.

Second, we use the following method to define the CS-GSD of amplitude part. We use a Laplace operator, i.e., second-order differential operator, to express the amplitude information as follows:

$$\Delta f = \nabla^2 f = \nabla \cdot \nabla f \tag{6}$$

where the notation ∇ is $(\partial f/\partial x, \partial f/\partial y)$. The Laplacian of f is the sum of all the unmixed second partial derivatives in the coordinates (x, y), In a 4×4 image block, (1) can be calculated as follows:

$$\Delta f = \Delta f_x + \Delta f_y = \sum_{x=1}^{4}\sum_{y=1}^{4}\left(\frac{\partial^2 f(x,y)}{\partial x^2}\right)^2 + \left(\frac{\partial^2 f(x,y)}{\partial y^2}\right)^2 \tag{7}$$

with

$$\frac{\partial^2 f(x,y)}{\partial x^2} = f(x+1,y) - 2f(x,y) + f(x-1,y) \tag{8}$$

$$\frac{\partial^2 f(x,y)}{\partial x^2} = f(x,y+1) - 2f(x,y) + f(x,y-1). \tag{9}$$

We used traces of matrix to express the CS-GSD of the amplitude part as follows:

$$\begin{aligned}\Delta f^2 &= \mathrm{trace}({K_3}^T K_3 F F^T) + \mathrm{trace}(F^T F K_4 {K_4}^T) \\ &= \mathrm{trace}(R_1 F F^T) + \mathrm{trace}(F^T F R_2) \\ &= \mathrm{trace}(R_1 F F^T) + \mathrm{trace}(R_1 F^T F) \\ &= \mathrm{trace}(R_1 F F^T + R_1 F^T F) = \mathrm{trace}(R_1 (F F^T + F^T F))\end{aligned} \tag{10}$$

where $K_3 = Ck_3C^T$, $K_4 = Ck_4C^T$, k_3=k_2–k_1, $k_4 = k_2^T$–k_1^T, k_1 and k_2 are two constant cyclic matrices, R_1 and R_2 are the constant parameters as: $R_1 = R_2 =$ (8 16 0 8; 16 40 8 32;0 8 40 16; 8 32 16 72). Therefore, the CS-GSD of the amplitude part can be obtained through transformed coefficients F. The total CS-GSD value can be calculated via (10) and (5).

We utilize a secondary transform to establish a CS-GS, which guides the allocation of sensing resources to different regions in a wavelet subband. We use P to express an image of the image sensor layer. The compression process is composed of the following steps.

1) Transform an image from the image sensor layer into wavelet subbands, and then organize wavelet coefficients of a subband into multiple block structure. The block structure is consistent with the measurement matrix structure of CS. Each wavelet subblock (WSB) size is 4×4 pixels and we use W_{i} to express a divided wavelet block (4×4 pixels).
2) We use every four WSBS as a CS block (CSB), which is expressed by $W = \{w_1, w_2, w_3, w_4\}$. The organized CSB could be seen as a new low-resolution wavelet image, where each pixel is a WSB block of 16 wavelet coefficients. In each CSB, We use the aforementioned CS-GSD algorithm to extract the CS-GS of each CSB. We use f_i $(w_i \rightarrow f_i)$ to express the secondary transformed coefficients. We use η_i to express the ith block of the CSB. The value of η_i is calculated as follows:
$$\eta_i = \frac{1}{L \times L} \sum_{m}^{L} \sum_{n}^{L} f(m, n) \tag{11}$$
where L is the size of the block η_j. Therefore, the total sensing resource guiding value of a CSB is calculated $T = \eta_1 + \eta_2 + \eta_3 + \eta_4$.
3) We use N to express the total number of the CSB. The sensing resource allocation of a CSB can be calculated as follows:
$$T_i = \frac{T_i}{\sum_{i=1}^{N} T_i} \times A \tag{12}$$
where A is the total sensing measurement number, which is determined by the bit-rate budget in a bit-rate controller.

III. Experiments

We test and analyze our proposed approach on a self-developed compression testing platform to verify its performance and feasibility. The testing platform includes an image simulation source, a compression system, a compression and storage server (CSS), a decoding unit, and a display system. The CSS is a remote sensing image database including plenty of remote sensing images with a variety of image sizes, contents, and resolutions. The CSS sends remote sensing images to the image simulation source unit. The image simulation source unit adjusts the output line frequency, image size, and output time to simulate the image-sensor output. The compression system compresses the received remote sensing image. The compression system uses a processor with the Virtex-PRO Xilinx FPGA including a 32-bit MicroBlaze. In the following experiments, all algorithms are implemented on the FPGA processor. The compressed streams are received and decoded by the decoding unit. The reconstructed image is transmitted to the compression and storage server.

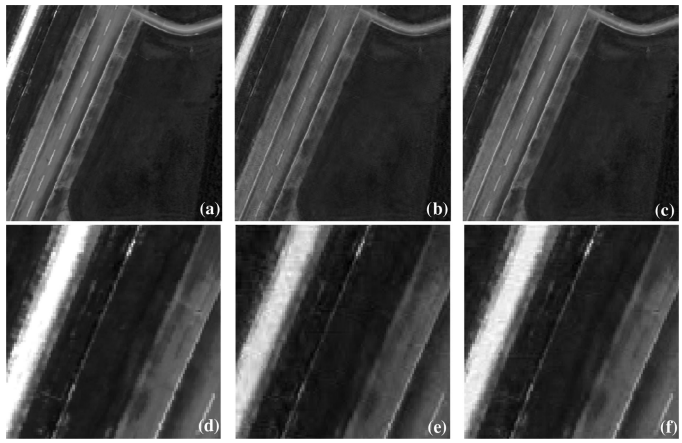

Fig. 2. Reconstructed results, (a) original image, (b) without secondary transform, (c) HCS, (d)-(f) the local regions of different images.

To evaluate the proposed method, we use different groups of remote sensing images from different satellites as test input. First, we use a Quickbird panchromatic image as the testing input. The bit depth is 8 bit. We use conventional wavelet-based CS (without secondary transform) as the reference method. Fig. 2 shows the three constructed image using different methods. From the reconstructed local region, the secondary transform reserves the edge information compared to the case when the secondary transform is not used.

We objectively evaluate the effects of the secondary transform on this set of images. We use two reference methods: conventional wavelet-based CS (without secondary transform) and wavelet-based method without CS. In the conventional wavelet-based CS, sensing sources are uniformly allocated to each CSB. The wavelet-based method uses a bit-plane coder from an SPIHT algorithm to compress images. We use two performance evaluation parameters: peak signal-to-noise ratio (PSNR) and mean structural similarity (MSSIM) [27]. The PSNR could reflect the quality of reconstruction of the compression algorithm. The MSSIM demonstrates the quality of the detailed information of the reconstructed images, such as textures and edges. Hundred Quickbird panchromatic images are used as the test input data, where each image has the bit depth of 8 bit and the size of 1024×1024 pixels. Fig. 3 shows the tested results of PSNR at 3.5–0.5 bpp. The proposed method can obtain the improvement of the PSNR compared with the conventional wavelet-based compressive sensing because our method can allocate more compressive sensing resources and fewer to zero areas. Fig. 4 shows the tested results of MSSIM. Our method obtained the best performance in the MSSIM values, which indicated that our method can keep the more texture information at same bit-rates compared with other methods.

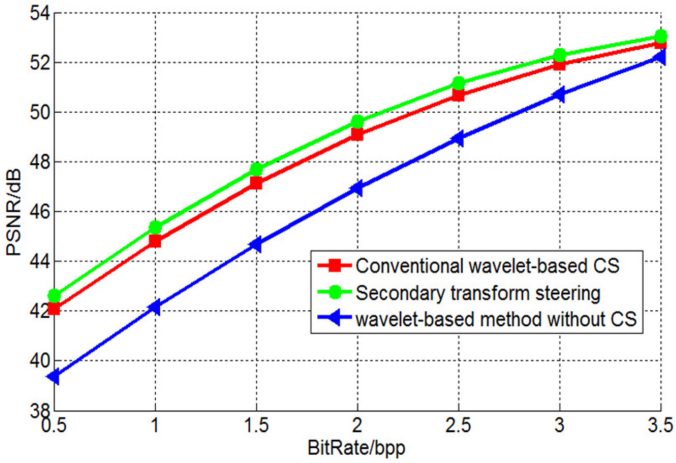

Fig. 3. Comparison of PSNR on Quickbird panchromatic images.

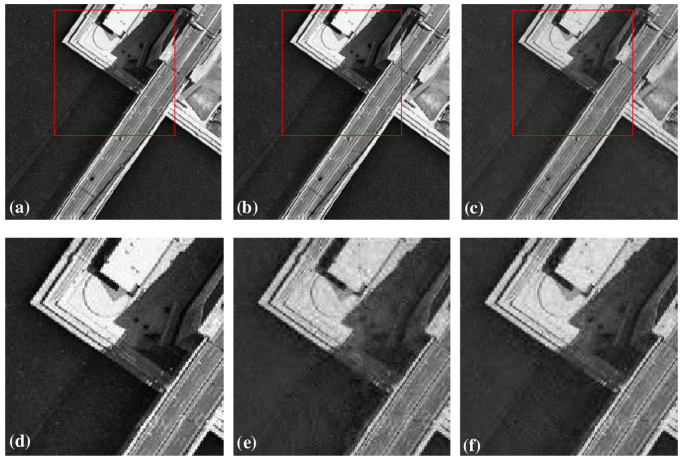

Fig. 5. Reconstructed results, (a) original image, (b) without secondary transform, (c) with secondary transform, (d)–(f) the local regions of different images.

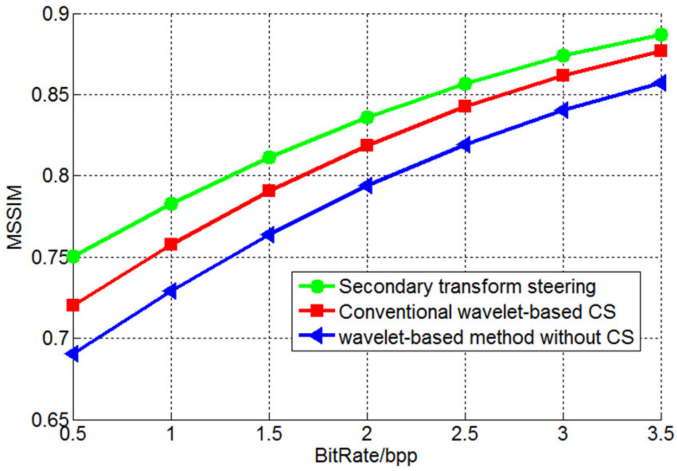

Fig. 4. Comparison of MSSIM on Quickbird panchromatic images.

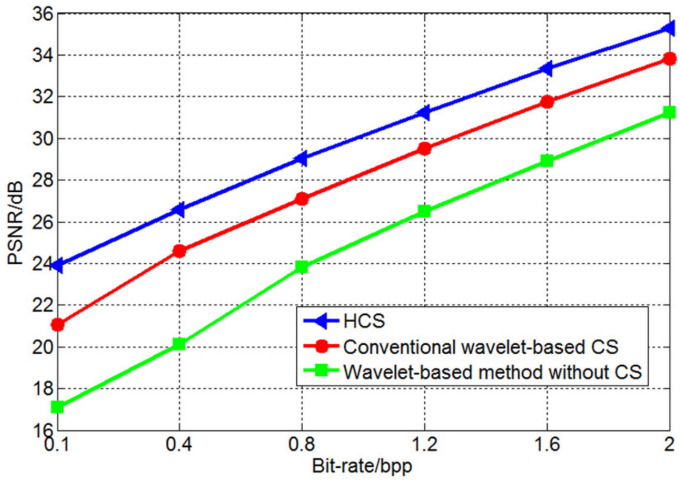

Fig. 6. Comparison of PSNR on ASTER remote sensing images.

Second, we also use ASTER remote sensing image gallery as test images to evaluate our method. The number of this set of images is 100 and the bit depth is 8 bit. We use conventional wavelet-based CS as the reference method. Fig. 5 shows the three constructed image using different methods. From the reconstructed local region, the secondary transform achieves the same results, reserving the edge information compared to the case when the secondary transform is not used. We also use the same performance parameters (PSNR and MSSIM) to evaluate the quality of reconstructed images and the quality of the detailed information (textures and edges) on this set of images. The reference methods are also conventional wavelet-based CS (without secondary transform) and wavelet-based combined with bit-plane coder method without CS. Fig. 6 shows the tested results of PSNR at 0.1–2 bpp. The proposed method can also obtain the improvement of the PSNR compared with the conventional wavelet-based compressive sensing because compressive sensing resources can be efficiently utilized in high-frequency areas. Fig. 7 shows the tested results of MSSIM. Our method also obtains the best performance in the MSSIM values, which demonstrates that our method can keep the more texture information at same bit-rates compared with other methods.

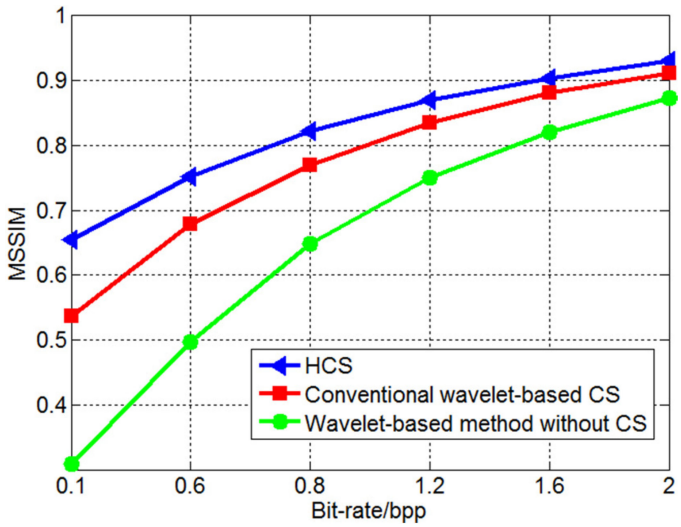

Fig. 7. Comparison of MSSIM on ASTER remote sensing images.

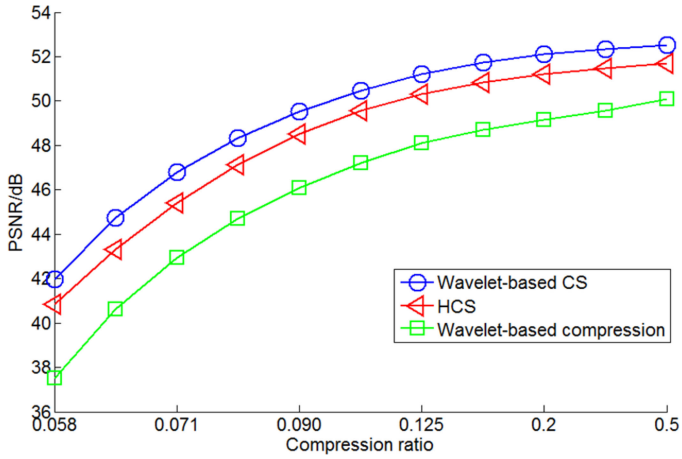

Fig. 8. Performance comparison of different compression methods.

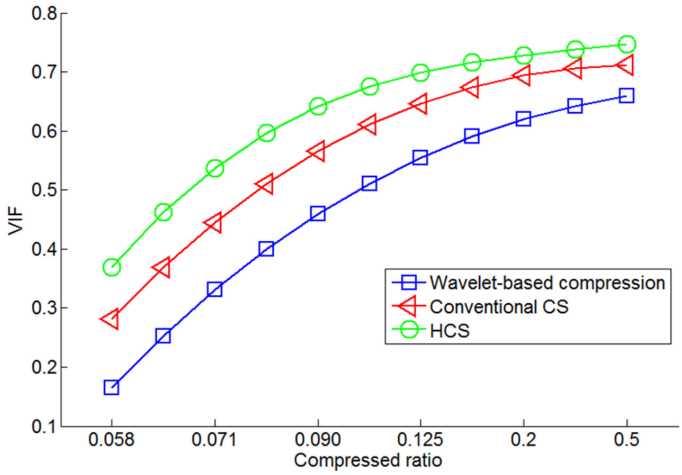

Fig.9. VIF values at different compression ratio.

Third, remote sensing images of urban buildings from IKONOS Earth observation satellite are used to evaluate our algorithm performance in compression times. The bit depth is 8 bit and the image number is 100. The size of images is 3072 $\times$ N, where N is the line number of tested images. We use conventional compressive sensing, the wavelet-based compression method as reference methods. We use PSNR and visual information fidelity (VIF) [28] as the performance evaluation parameters in this experiment. The VIF is based on the hypothesis that the human visual system is highly adopted for extracting the structure information. Fig. 8 shows the tested results of PSNR difference between methods. The results indicated that the PSNR of our method can obtain the higher PSNR than other methods. VIF values at different compressed ratio are shown in Fig. 9. Because we use a secondary transform to guide the allocation of posttransform resources and bit-rate resources, our method outperforms the traditional methods in the PSNR and VIF. Fig. 10 shows the comparison results of the compression time for different compression algorithms. The processing time of our algorithm is less than conventional wavelet-based compression method. Although the compression time of this proposed method is slightly higher than the conventional CS, the compression performance is higher than conventional CS.

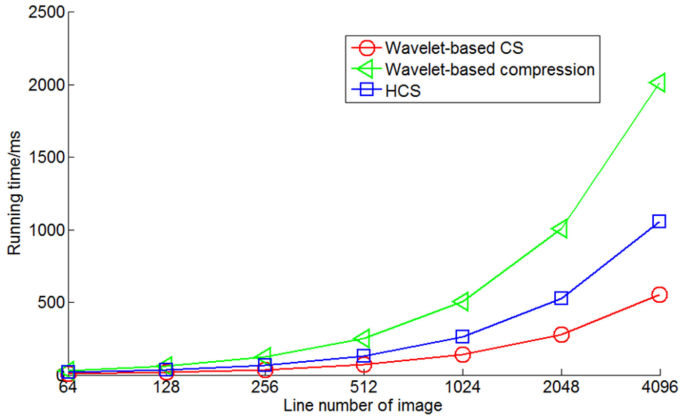

Fig. 10. Compression time of different compression algorithms.

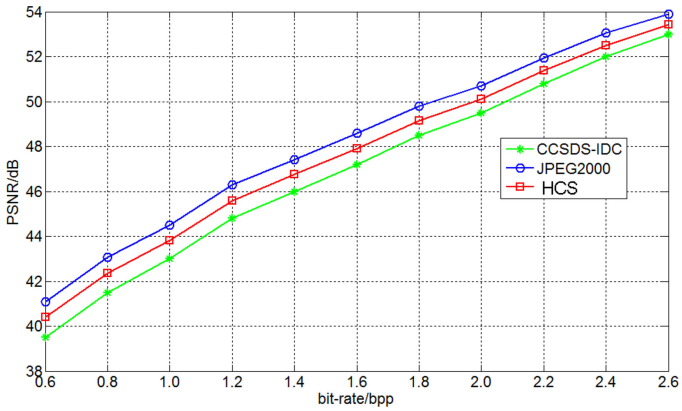

Fig. 11. Comparison to the compression standards.

This method is a nice tradeoff between the complexity and compression performance.

In addition, remote sensing image sets from Quickbirdand IKONOS Earth observation satellites, including a variety of ground objects, such as cities, sea, and mounts, which are used to compare our algorithm performance with the compression standards, JPEG2000 and CCSDS-IDC (CCSDS 122.0-B-1). The bit depth of each pixel is 8 bit and the image size is 1024 $\times$ 1024 pixels. Fig. 11 compares the performance of the three compression methods. In JPEG2000, EBCOT adopts a contextual adaptive arithmetic coder, called MQ-coder, with a rate-distortion optimization process to sort the code-blocks in the best order. In CCSDS-IDC (CCSDS 122.0-B-1), the BPE utilizes the structures of SOTs on a bit plane. On a given bit-plane of an SOT, grandchildren coefficients also become nonsignificant when children coefficients are nonsignificant. The bit planes in SOT include large zero areas, which can be utilized to improve the coding efficiency. From Fig. 11, the JPEG2000 method has the best compression performance and the proposed method improved the PSNR of 0.9–0.4 dB at 0.6–2.6 bpp comparing with CCSDS-IDC (CCSDS 122.0-B-1).

Finally, the complexity of the proposed method is analyzed. The encoding stage of the proposed method includes a wavelet transform, a secondary HT transform, CS-GSD calculation, and CS sensing measurement, and entropy encoding. The secondary HT has very low complexity because the Hadamard basis includes simple additions and subtractions of wavelet coefficients without any multiplication. The CS-GSD calculation uses 4 $\times$ 4

TABLE I
RESULTS OF COMPLEXITY COMPARISON

Methods	Complexity
The proposed method	0.051μs/sample
JPEG2000	0.53μs/sample
CCSDS-IDC (CCSDS 122.0-B-1)	0.34μs/sample

matrix multiplication operations, which have the calculation complexity of O(64). In the CS sensing measurement stage, $N \times N$ image block has the calculation complexity of $O(N^2M)$. In the JPEG2000 algorithm, a wavelet transform, embedded block coding with optimization truncation and entropy encoding. However, embedded block coding with optimization truncation is an optimized calculation process and has very high complexity. The CCSDS method uses the BPE except for the wavelet transform and entropy encoding. The BPE is a zero-tree encoder and needs to scan each bit-plane. The BPE also has the high calculation complexity. Compared with the JPEG2000 and CCSDS-IDC (CCSDS 122.0-B-1), the proposed method has very low complexity. We test the calculation complexity of the proposed compression method with compression times. The Virtex-PRO Xilinx FPGA with the MicroBlaze is utilized to implement the proposed algorithm for evaluating the compression time. Table I compares the results of the compression complexity for different compression algorithms. The processing time of the proposed algorithm is 0.051 μs/sample, which indicates less time than other methods in [29] and [30]. The compression time of 128 $\times$ 3072 needs only 20.05 ms. The compression algorithm is not optimized for FPGA implementation, where the compression system has the main frequency of 100 MHz, occupying slices of 74% (25006/33792), 4 input LUTs of 71% (47984/67584), and BRAM of 82% (118/144). According to the different principles of TDICCD imaging, the proposed compression algorithm can be optimized on an FPGA. An optimized implementation on an FPGA can take minimal time.

Based on the above experimental results, the proposed method has the high compression performance and very low complexity, which is very suitable for the onboard compressor applications. The reconstructed quality of the proposed method depends on the reconstruction algorithm. In the future, we will use current advanced technologies, such as deep learning, to investigate the recovery algorithm for obtaining the better reconstruction quality.

IV. CONCLUSION

In this paper, we propose a new remote sensing image compression method with HCS, which utilizes a secondary transform in the wavelet domain to steer the allocation of the sensing resources. The low-frequency areas (having a number of zeros areas) use relatively small sensing resources, while more sensing resources shift to the high-frequency area, enabling the high reconstruction quality as well as high compression performance at same compression conditions. The experimental results on multiple sets of remote sensing images confirm that this method obtains the better compression performance compared with the conventional CS method. This method can be especially used for visible/near-infrared images but in principle also for multispectral and hyperspectral images.

REFERENCES

[1] H. Li, W. Ding, X. Cao, and C. Liu, "Image registration and fusion of visible and infrared integrated camera for medium-altitude unmanned aerial vehicle remote sensing," *Remote Sens.*, vol. 9, no. 5, 2017, Art. no. 441.

[2] C. Wang *et al.*, "Optical flow inversion for remote sensing image dense registration and sensor's attitude motion high-accurate measurement," *Math. Problems Eng.*, vol. 2014, 2014, Art. no. 432613.

[3] J. Li, F. Liu, S. Liu, and Z. Wang, "Optical remote sensor calibration using micromachined multiplexing optical focal planes," *IEEE Sens. J.*, vol. 17, no. 6, pp. 1663–1672, Mar. 2017.

[4] J. Li, Z. Liu, and F. Liu, "Using sub-resolution features for self-compensation of the modulation transfer function in remote sensing," *Opt. Express*, vol. 25, no. 4, pp. 4018–4037, 2017.

[5] D. Wang, T. Zhang, and H. Kuang, "Clocking smear analysis and reduction for multi phase TDI CCD in remote sensing system," *Opt. Express*, vol. 19, no. 6, pp. 4868–4880, 2011.

[6] L. I. E. R. Ph, G. Moury, C. Latry, and F. Cabot, "Selection of the SPOT5 image compression algorithm," *Proc. SPIE*, vol. 3439, pp. 541–552, 1998.

[7] C. Lambert-Nebout and G. Moury, "A survey of on-board image compression for CNES space missions," in *Proc. Int. IEEE Geosci. Remote Sens. Symp.*, 1999, vol. 4, pp. 2032–2034.

[8] J. Li, "A highly reliable and super-speed optical fiber transmission for hyper-spectral SCMOS camera," *Optik*, vol. 127, no. 3, pp. 1532–1545, 2016.

[9] J. Li, F. Liu, and Z. Liu, "Efficient multi-bands image compression method for remote cameras," *Chin. Opt. Lett.*, vol. 15, no. 2, 2017, Art. no. 022801.

[10] J. Li, F. Xing, and Z. You, "An efficient image compressor for charge coupled devices camera," *Sci. World J.*, vol. 2014, 2014, Art. no. 840762.

[11] L. Jin, J. Long-Xu, and Z. Ran-Feng, "An image compression method for space multispectral time delay and integration charge coupled device camera," *Chin. Phys. B*, vol. 22, no. 6, 2013, Art. no. 064203.

[12] E. J. Candès and M. B. Wakin, "An introduction to compressive sampling," *IEEE Signal Process. Mag.*, vol. 25, no. 2, pp. 21–30, Mar. 2008.

[13] W. Dai and O. Milenkovic, "Subspace pursuit for compressive sensing signal reconstruction," *IEEE Trans. Inf. Theory*, vol. 55, no. 5, pp. 2230–2249, May 2009.

[14] J. Ma, "Single-pixel remote sensing," *IEEE Geosci. Remote Sens. Lett.*, vol. 6, no. 2, pp. 199–203, Apr. 2009.

[15] J. Bobin, J. L. Starck, and R. Ottensamer, "Compressed sensing in astronomy," *IEEE J. Sel. Topics Signal Process.*, vol. 2, no. 5, pp. 718–726, Oct. 2008.

[16] J. Li and Z. Liu, "Efficient compressed imaging method for a microsatellite optical camera," *Appl. Opt.*, vol. 55, no. 28, pp. 8070–8081, 2016.

[17] J. Ma and F. X. Le Dimet, "Deblurring from highly incomplete measurements for remote sensing," *IEEE Trans. Geosci. Remote Sens.*, vol. 47, no. 3, pp. 792–802, Mar. 2009.

[18] C. Li, T. Sun, K. F. Kelly, and Y. Zhang, "A compressive sensing and unmixing scheme for hyperspectral data processing," *IEEE Trans. Image Process.*, vol. 21, no. 3, pp. 1200–1210, Mar. 2012.

[19] D. Venkatraman and A. Makur, "A compressive sensing approach to object-based surveillance video coding," in *Proc. IEEE Int. Conf. Acoustics, Speech Signal Process.*, Apr. 2009, pp. 3513–3516.

[20] J. Wen, Z. Chen, Y. Han, J. D. Villasenor, and S. Yang, "A compressive sensing image compression algorithm using quantized DCT and noiselet information," in *Proc. IEEE Int. Conf. Acoustics Speech Signal Process.*, Mar. 2010, pp. 1294–1297.

[21] C. Deng, W. Lin, B. S. Lee, and C. T. Lau, "Robust image compression based on compressive sensing," in *Proc. IEEE Int. Conf. Multimedia Expo*, Jul. 2010, pp. 462–467.

[22] C. Deng, W. Lin, B. S. Lee, and C. T. Lau, "Robust image coding based upon compressive sensing," *IEEE Trans. Multimedia*, vol. 14, no. 2, pp. 278–290, Apr. 2012.

[23] J. Hahn, C. Debes, M. Leigsnering, and A. M. Zoubir, "Compressive sensing and adaptive direct sampling in hyperspectral imaging," *Digital Sig. Process.*, vol. 26, pp. 113–126, 2014.

[24] A. Rajwade, D. Kittle, T. H. Tsai, D. Brady, and L. Carin, "Coded hyperspectral imaging and blind compressive sensing," *SIAM J. Imag. Sci.*, vol. 6, no. 2, pp. 782–812, 2013.

[25] X. Lin, Y. Liu, J. Wu, and Q. Dai, "Spatial-spectral encoded compressive hyperspectral imaging," *ACM Trans. Graphics*, vol. 33, no. 6, 2014, Art. no. 233.

[26] S. Yang, M. Wang, P. Li, L. Jin, B. Wu, and L. Jiao, "Compressive hyperspectral imaging via sparse tensor and nonlinear compressed sensing," *IEEE Trans. Geosci. Remote Sens.*, vol. 53, no. 11, pp. 5943–5957, Nov. 2015.
[27] Z. Wang, A. C. Bovik, H. R. Sheikh, and E. P. Simoncelli, "Image quality assessment: From error visibility to structural similarity," *IEEE Trans. Image Process.*, vol. 13, no. 4, pp. 600–612, Apr. 2004.
[28] H. R. Sheikh and A. C. Bovik, "Image information and visual quality," *IEEE Trans. Image Process.*, vol. 15, no. 2, pp. 430–444, Feb. 2006.
[29] J. Liu and P. Moulin, "Information-theoretic analysis of interscale and intrascale dependencies between image wavelet coefficients," *IEEE Trans. Image Process.*, vol. 10, no. 11, pp. 1647–1658, Nov. 2001.
[30] V. K. Goyal, "Theoretical foundations of transform coding," *IEEE Signal Process. Mag.*, vol. 18, no. 5, pp. 9–21, Sep. 2001.

Jin Li was born in 1984. He received the Ph.D. degree from the University of Chinese Academy of Sciences, Beijing, China, in 2013.

He is currently a Postdoctoral Fellow with the Department of Engineering, University of Cambridge, Cambridge, U.K. His research interests include high dynamic optical imaging, optical sensors, and image processing technology.

Yao Fu received the Ph.D. degree from Changchun Institute of Optics, Fine Mechanics and Physics, Chinese Academy of Sciences, Changchun, China, in 2012.

She is currently an Associate Professor with Changchun Institute of Optics, Fine Mechanics and Physics, Chinese Academy of Sciences. Her research interests include remote sensing optical imaging and image processing.

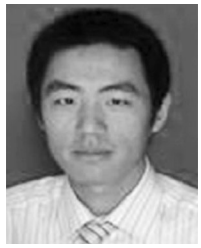

Guoning Li received the Ph.D. degree from Changchun Institute of Optics, Fine Mechanics and Physics, Chinese Academy of Sciences, Changchun, in 2008.

He is currently a Professor with Changchun Institute of Optics, Fine Mechanics and Physics, Chinese Academy of Sciences. His research interests include remote sensing image acquisition and image processing.

Zilong Liu received the Ph.D. degree from Beijing Institute of Technology, Beijing, China, in 2013.

He is currently an Associate Professor with the Optical Division, National Institute of Metrology, Beijing. His research interests include high dynamic optical imaging, optical sensors, and image processing technology.